Materials Advances

ROYAL SOCIETY OF CHEMISTRY

PAPER

View Article Online
View Journal | View Issue

Cite this: *Mater. Adv.*, 2025, 6, 2385

Advanced dual-mode Er^{3+}/Yb^{3+} phosphors for high-precision optical thermometry across broad temperature ranges†

Zein El Abidine Aly Taleb, [a] Ikhlas Kachou,[a] Kamel Saidi, [ab] Mohamed Dammak, *[a] Irene Mediavilla[c] and Juan Jiménez[c]

Dual-mode light-emitting phosphors play a vital role in advanced technologies and functions as they constitute optical thermometers for a wide range of temperature environments. This study presents a novel Er^{3+}/Yb^{3+} co-doped $NaCaY(MoO_4)_3$ (NCYM) phosphor synthesized *via* the sol–gel method for precise optical thermometry across a broad temperature range (300–510 K). The research includes an in-depth analysis of the crystal structure, morphology, optical properties, and decay kinetics. The luminescence mechanism and energy transfer processes were elucidated, with NCYM:Er^{3+}/Yb^{3+} phosphors efficiently activated under 980 nm and 325 nm laser excitation. These excitations produced $^2H_{11/2}/^4S_{3/2} \rightarrow {}^4I_{15/2}$ transitions *via* up-conversion (UC) and down-conversion (DC) mechanisms, respectively. A dual-mode optical thermometry system was developed, combining DC and UC approaches for simultaneous evaluation. At 300 K, the maximum relative sensitivities ($S_{r\text{-}max}$) were 1.2% K^{-1} (DC) and 1.045% K^{-1} (UC), while at 510 K, the maximum absolute sensitivities ($S_{a\text{-}max}$) reached 15.17 × 10^{-3} K (DC) and 12.15 × 10^{-3} K (UC). The system demonstrated exceptional temperature resolution, with uncertainties (δT) below 0.313 K, covering the full range of 300 to 510 K. This work positions NCYM:Er^{3+}/Yb^{3+} phosphors as highly promising materials for precise optical temperature sensing in a variety of advanced applications.

Received 7th February 2025,
Accepted 8th March 2025

DOI: 10.1039/d5ma00108k

rsc.li/materials-advances

1. Introduction

Temperature is a necessary parameter that affects many aspects of daily life, including industry, aerospace, bioengineering, infrared detectors, scientific research activities, and other areas.[1–3] Initially, traditional contact-based temperature measurement methods were employed, relying on the expansion and contraction of liquids (typically mercury) in response to temperature changes.[4,5] However, these techniques have limitations, especially in challenging environments such as fast-moving objects, high-temperature reactors, and underground mines.[6–8] Consequently, traditional methods are becoming increasingly inadequate for the needs of evolving technologies, driving a transition toward non-contact temperature measurement techniques. These innovative approaches allow remote temperature monitoring, in contrast to the limitations of direct-contact thermometers.

Luminescent materials capable of both down-conversion (DC) and up-conversion (UC) processes have garnered significant interest due to their wide-range of applications. In DC processes, high-energy photons are absorbed and re-emitted as lower-energy photons, whereas UC processes involve the absorption of multiple low-energy photons to emit a higher-energy photon. Rare-earth (RE) luminescent materials, particularly Er^{3+}/Yb^{3+} co-doped hosts, are frequently explored for their ability to facilitate these processes through efficient energy transfer between Yb^{3+} and Er^{3+} ions.

In recent studies, we have systematically investigated the potential of Yb/Ln^{3+} ion couples across various applications, with a special focus on their utility in optical thermometry. Notably, our first series of articles[9–12] explored the broad applicability and versatility of these couples in diverse material systems. Building on this foundation, the second ensemble of our work specifically delved into the exceptional performance and unique advantages of the Er/Yb pair in advanced optical sensing and high-precision thermometry applications.[13–21] Together, these investigations underscore the critical role of Yb/Ln^{3+} dopant combinations in advancing functional materials for next-generation technologies.

[a] *Laboratoire de Physique Appliquée, Faculté des Sciences de Sfax, Département de Physique, Université de Sfax, BP 1171 Sfax, Tunisia.*
E-mail: madidammak@yahoo.fr, mohamed.dammak@fss.usf.tn
[b] *Department of Physics, Sfax Preparatory Engineering Institute, University of Sfax, 1172-3000 Sfax, Tunisia*
[c] *GdS Optronlab, Department of Condensed Matter Physics, University of Valladolid, LUCIA Building, Paseo de Belén 19, Valladolid, 47011, Spain*

† Electronic supplementary information (ESI) available. See DOI: https://doi.org/10.1039/d5ma00108k

The photoluminescence behavior of RE elements is primarily determined by intra-4f electronic transitions. Er^{3+} ions are especially desirable for UC and DC luminescence due to their multiple metastable energy states and wide emission spectra, including visible emissions at 550 nm and 670 nm, as well as near-infrared (NIR) emissions at 800 nm. Nonetheless, the inherently low absorption cross-section of Er^{3+} ions poses a challenge, limiting the efficiency of direct photon absorption in both UC and DC processes.

Yb^{3+} ions are commonly selected as sensitizers for UC processes due to their high absorption cross-section at 980 nm. This choice enhances the efficiency of detecting the green emission from Er^{3+} ions when excited at this wavelength. The energy states of Er^{3+}, particularly $^2H_{11/2}$ and $^4S_{3/2}$, are separated by approximately 700 to 800 cm^{-1}, facilitating efficient non-radiative transitions and contributing to their distinct luminescence properties,[22,23] leading to a Boltzmann-type distribution of these states. This makes the $^2H_{11/2} \rightarrow {}^4I_{15/2}$ and $^4S_{3/2} \rightarrow {}^4I_{15/2}$ transitions ideal for luminescent ratiometric thermal detection.

Optical temperature parameters are determined using Boltzmann's distribution law and the fluorescence intensity ratio (LIR) technique, applied to two thermally coupled energy levels (TCL) with an energy gap of less than 2000 cm^{-1}.[24–26]

The choice of a host material is also important, as it influences the emission color through the varying lattice environments. The UC process is strongly affected by the host lattice properties and its interaction with doped rare-earth ions.[27–29] Molybdate compounds have garnered interest as fluorescent media due to their broad and intense absorption bands, high emission intensity, and excellent dispersibility of RE ions.[30,31] Recently, NCYM has gained attention as a host material for RE-ion-doped phosphors, offering good physical and chemical stability, low cutoff phonon energy, and high solubility for RE ions, making it ideal for solid-state applications.

We selected NCYM as the host material in our study due to its potential for enhanced detection performance, tunable optical properties, and the opportunity to explore a novel material system. The incorporation of supplementary elements, specifically sodium (Na), calcium (Ca), and yttrium (Y), introduces additional energy levels and modifies the host lattice's properties. This enables finer control over luminescence behavior and improves detection capabilities. When compared to existing systems (*e.g.*, $SrTiO_3:Er^{3+}/Yb^{3+}$,[32] $SrTiO_3:Er^{3+}$,[33] $CaTiO_3:Er^{3+}/Yb^{3+}$,[34] $CaTiO_3:Er^{3+}$,[35] $Ca_3Y_2Ge_3O_{12}:Er^{3+}/Yb^{3+}$,[36] $Sr_2YTaO_6:Er^{3+}$, Yb^{3+} [37] and $SrWO_4:Er^{3+}/Yb^{3+}$ [38]), the Er^{3+}/Yb^{3+}-co-doped NCYM material system emerges as a promising candidate for precise optical temperature sensing applications.

In this study, NCYM:Er^{3+}/Yb^{3+} phosphors were excited using both 980 nm and 325 nm lasers. The green emission from Er^{3+} ions, corresponding to the $^2H_{11/2} \rightarrow {}^4I_{15/2}$ and $^4S_{3/2} \rightarrow {}^4I_{15/2}$ transitions, was observed for both excitation wavelengths. These emissions resulted from up-conversion and down-conversion processes, respectively. The thermometric properties of the NCYM:Er^{3+}/Yb^{3+} phosphors were systematically evaluated under both excitation conditions, with key temperature sensor parameters, such as relative sensitivity and temperature resolution, being compared. This study emphasizes the development of advanced luminescent thermometers with outstanding relative sensitivity, leveraging the unique properties of Er^{3+}/Yb^{3+} co-doped NCYM materials.

2. Experimental section

2.1 Materials

The starting materials used for the synthesis of NCYM:$0.02Er^{3+}/0.2Yb^{3+}$ phosphors included sodium nitrate ($NaNO_3$, 99.0%), calcium nitrate tetrahydrate ($Ca(NO_3)_2{\cdot}4H_2O$, 99.0%), yttrium(III) nitrate hexahydrate ($Y(NO_3)_3{\cdot}6H_2O$, 99.9%), erbium nitrate pentahydrate ($Er(NO_3)_3{\cdot}5H_2O$, 99.9%), ytterbium nitrate pentahydrate ($Yb(NO_3)_3{\cdot}5H_2O$, 99.9%), ammonium molybdate tetrahydrate ($(NH_4)_6Mo_7O_{24}{\cdot}4H_2O$, 99.9%), and citric acid ($C_6H_8O_7$, 99.0%). All chemical reagents were obtained from Sigma-Aldrich and used as received, without further purification.

2.2 Sample synthesis

The sol–gel method was employed to synthesize Er^{3+}/Yb^{3+} co-doped $NaCaY(MoO_4)_3$ (NCYM). Initially, stoichiometric amounts of sodium nitrate, calcium nitrate tetrahydrate, yttrium nitrate hexahydrate, erbium nitrate pentahydrate, ytterbium nitrate pentahydrate, and ammonium molybdate tetrahydrate were dissolved in 200 mL of deionized water. To facilitate complexation, 5 mol of citric acid was added as a chelating agent, maintaining a citric acid to metal ion ratio of 1 : 2. The resulting mixture was stirred for one hour at room temperature, producing a solution that changed color from transparent to blue as it was heated. As the reaction progressed, a blue wet gel began to form. The stopper was then removed, allowing the liquid to evaporate. The gel was dried in an oven at 423 K for 12 hours, resulting in a stable, porous xerogel. This xerogel was subsequently annealed at 673 K for 3 hours, yielding black particles. Finally, the sample was sintered in air at 973 K for 3 hours, resulting in the formation of pure-phase crystalline particles. This technique was utilized to make NCYM structures doped with the following doping ion concentrations: $20\%Yb^{3+}/2\%Er^{3+}$. To prevent UC luminescence quenching, we utilized certain quantities of dopant ions based on our experience and general understanding. Indeed, for UC systems, 20% sensitizer (Yb^{3+}) and low concentrations of emitters (around 2%) are commonly employed, since they are appropriate conditions that typically result in strong UC for strong emission.[17,18,39,40]

3. Characterization techniques

X-ray powder diffraction (PXRD) patterns were obtained at room temperature using a Bruker D8-Advance X-ray powder diffractometer, with monochromatic CuKa1 copper radiation (1.5406 Å) in the range of 5–70 degrees 2θ. The morphology of the samples was examined using a Zeiss Supra55VP FEG-SEM field emission scanning electron microscope and a Bruker XFlash 5030 detector. The photoluminescence (PL) spectra were recorded using a He–Cd laser (325 nm) with a Labram UV-HR

800 Raman spectrometer (Horiba-Jobin Yvon) equipped with a low-dispersion 150 g mm^{-1} grating. Emission spectra were also obtained under excitation with a diode laser (980 nm) at a constant pump power of 30 mW. These measurements were carried out using a monochromator (Horiba Jobin Yvon, iHR320) equipped with an 1800 g mm^{-1} grating blazed at 500 nm and a photomultiplier tube (Hamamatsu, R928) to detect luminescence in the green–red spectral window. The chemicals and equipment used for this study were sourced through the facilities of the University of Valladolid, Spain, and the University of Sfax, Tunisia.

4. Result and discussion

4.1 X-ray diffraction analysis

X-ray diffraction (XRD) patterns were used to study the crystal structure and phase purity of the samples. Fig. 1 shows XRD patterns of NCYM:Er^{3+}/Yb^{3+} nanocrystals in the 5–70 $2\theta^{\circ}$ range. All diffraction peaks in the XRD curves are easily indexed to a pure tetragonal phase with a scheelite structure. Its powder X-ray diffraction (PXRD) pattern matches the standard Joint Committee on Powder Diffraction Standards (JCPDS 25-0828). There are no impurity diffraction peaks observed, which suggests that Er^{3+}/Yb^{3+} ions were successfully incorporated at the Y^{3+} sites and the obtained sample is composed of the pure molybdate structure. The Rietveld refinement was used to check the phase purity (Fig. S1, ESI†) and determine the unit cell parameters, which are listed in Table S1 (ESI†), confirming the phase purity of the synthesized material. X-ray powder diffraction (XRPD) was employed for structural analysis.

Considering the similar ionic radii of Y^{3+} (1.019 Å, C.N. = 8), Er^{3+} (1.004 Å, C.N. = 8) and Yb^{3+} (0.985 Å, C.N. = 8),[41,42] Er^{3+} and Yb^{3+} ions are most likely to replace Y^{3+} ions and enter the Er^{3+} and Yb^{3+} positions. As known, for a new solid-state solution, the radius percentage difference (D_r) between the potential substituted ions and dopants should be less than 30% by using

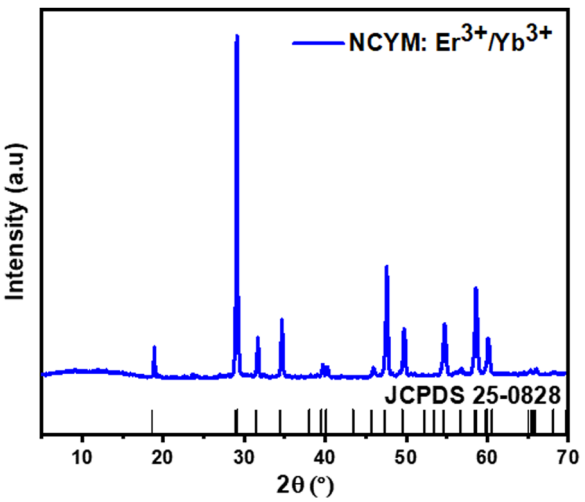

Fig. 1 The XRD pattern of the NCYM:Er^{3+}/Yb^{3+} phosphor.

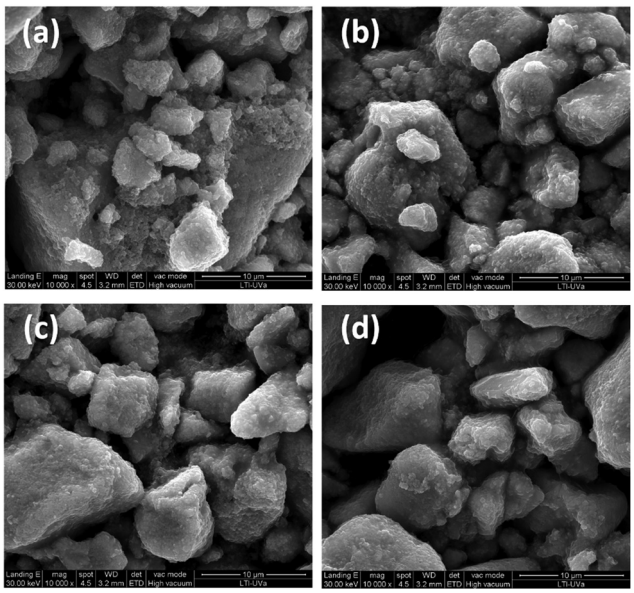

Fig. 2 (a)–(d) SEM images of the NCYM:Er^{3+}/Yb^{3+} sample.

eqn (1):[43]

$$D_r = \frac{R_S - R_D}{R_S} \times 100 \quad (1)$$

where R_S and R_D refer to the effective ionic radii of substituted cations and dopants, respectively. Using eqn (1), the D_r values of Y^{3+}/Er^{3+} and Y^{3+}/Yb^{3+} were estimated to be ≈1.47% and 3.33%, respectively. These calculated D_r values indicate that Er^{3+} and Yb^{3+} ions can easily enter into the NCYM host lattice by substituting Y^{3+} ions, as the D_r values are much smaller than 30%.

The morphology of the phosphors was also investigated by SEM, as shown in Fig. 2(a)–(d). It can be seen clearly from the images that the particles are well formed, with a homogeneous morphology and a size of about 1–2 μm. In general, the tightly packed particles contribute to a reduction in light scattering, which ultimately results in a high luminous efficiency. During the calcination process, the crystallites are of nanoscale size and therefore they have high surface energy. This causes the particles to agglomerate into larger structures and, finally, bulk materials.[9,44,45]

4.2 Photoluminescence properties

4.2.1 UV-visible spectroscopy and photoluminescence excitation (PLE) analysis. Fig. 3(a) displays the UV-vis-NIR diffuse reflectance spectra of NCYM:Er^{3+}/Yb^{3+}. The NCYM:Er^{3+}/Yb^{3+} sample exhibits strong host absorption in the UV region, centered at 313 nm, which is attributed to the charge transfer band (CTB) of Mo–O. In addition to these broad CTB bands, several peaks are observed at 522 nm, 654 nm, and 800 nm, corresponding to the transitions from the ground state $^4I_{15/2}$ to various excited states, namely $^2H_{11/2}$, $^4F_{9/2}$, and $^4I_{9/2}$ of Er^{3+} ions, respectively, as shown in Fig. 3(a). The absorption peak around 976 nm is assigned to the $^2F_{7/2} \rightarrow {}^2F_{5/2}$ transition of the Yb^{3+} ion.

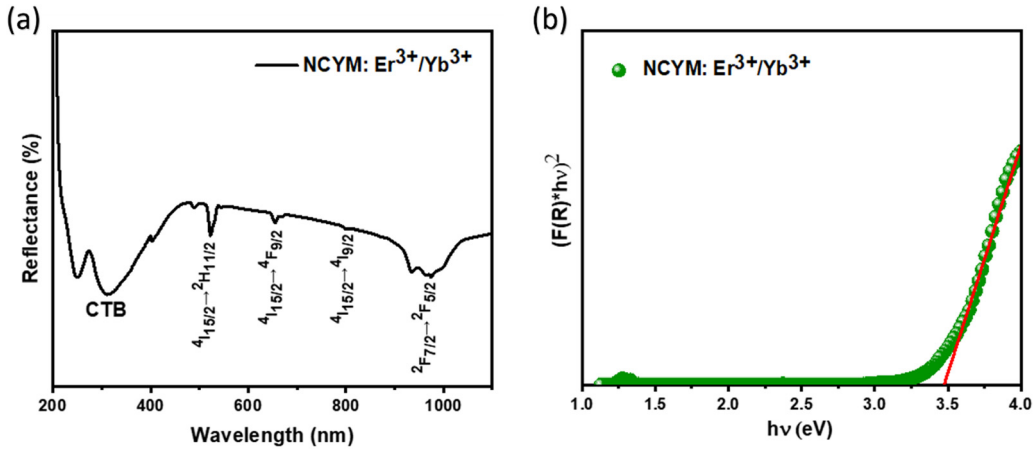

Fig. 3 (a) Diffuse reflectance spectra and (b) the plot of $[F(R)h\nu]^2$ *versus* $(h\nu)$ of NCYM:Er^{3+}/Yb^{3+}.

The plots of $[F(R_\infty)h\nu]^2$ *versus* photon energy $(h\nu)$ for NCYM:Er^{3+}/Yb^{3+} are shown in Fig. 3(b). The direct optical bandgap values (E_g) can be determined using the Kubelka–Munk (K–M) function and Tauc's relationship:[45,46]

$$F(R_\infty) = \frac{(1-R_\infty)^2}{2R_\infty} = \frac{K}{S} \quad (2)$$

$$[F(R_\infty)h\nu] = B(h\nu - E_g)^n \quad (3)$$

where R_∞ is the ratio of the light scattered from the sample and $F(R_\infty)$ is the K–M function; S is the scattering coefficient; K is the absorption coefficient; $h\nu$ is the the photon energy, E_g is the bandgap energy and n is a parameter that defines the nature of the band transition. The value of n is 1/2 for direct allowed transitions and 2 for indirect allowed transitions. Previous studies have confirmed that NCYM is a direct bandgap material. The optical bandgap values for the NCYM:Er^{3+}/Yb^{3+} samples were determined to be 3.46 eV, indicating that the incorporation of Er^{3+}/Yb^{3+} ions has a minimal influence on the bandgap value.

Fig. S2 (ESI†) shows the photoluminescence excitation (PLE) spectrum of NSGM:Er^{3+}/Yb^{3+} microcrystals, measured by monitoring the emission at 550 nm. This spectrum reveals a broad excitation band along with several narrow peaks. The broad band, ranging from 250 to 348 nm with a maximum centered around 300 nm, is attributed to the charge transfer band (CTB). The narrow peaks observed at approximately 365, 378, 406, 451, and 488 nm correspond to the 4f–4f transitions of Er^{3+} ions, from the ground state $^4I_{15/2}$ to the excited states $^4G_{9/2}$, $^4G_{11/2}$, $^2H_{9/2}$, $^4F_{5/2}$, and $^4F_{7/2}$, respectively. This novel phosphor can be excited well by using a UV source (250–348 nm).

4.2.2 Down/up-conversion emission studies of Er^{3+}/Yb^{3+} co-doped NCYM. To examine the down-conversion (DC) emission behavior of the synthesized phosphorescent material, the emission spectrum was recorded at an excitation wavelength of λ_{ex} = 325 nm, covering the range of 475–850 nm, as shown in Fig. 4(a). The down-conversion spectrum exhibits two distinct bands: a green emission peaking at 533 nm and 553 nm, which corresponds to the mixed transition $^2H_{11/2} + {}^4S_{3/2} \rightarrow {}^4I_{15/2}$, and a relatively weaker red band centered at 657 nm, indicating energy transfer from the NCYM crystals to the Er^{3+} ions.[26,47] The UC emission spectra of the sample was measured under laser excitation at 980 nm in the 475–850 nm wavelength regions (Fig. 4(b)). The UC spectra showed two distinct emission bands corresponding to the green and red emission of Er^{3+} ions. The green bands were centered on 533 and 553 nm, corresponding to the $^2H_{11/2} \rightarrow {}^4I_{15/2}$ and $^4S_{3/2} \rightarrow {}^4I_{15/2}$ transitions respectively. The red emission, located around 657 nm, is associated with the $^4F_{9/2} \rightarrow {}^4I_{15/2}$ transition of Er^{3+} ions. In addition to these peaks, there is also an emission around 800 nm, attributed to the $^4I_{9/2} \rightarrow {}^4I_{15/2}$ transition of the Er^{3+} ion.[48]

The color coordinates of the phosphors were calculated using the CIE chromaticity diagram,[49,50] which is shown in Fig. 4(c) and (d). In addition, under both 325 nm and 980 nm laser excitations, the final color is green, with CIE chromaticity coordinates: (x = 0.2339, y = 0.7414) and (x = 0.2736, y = 0.6947) for DC and UC, respectively. These coordinates are calculated based on the corresponding DC and UC emission spectra measured under ambient conditions (Fig. 3a and b). The CCT of the phosphor material is equal to the temperature of an ideal body radiator that emits light of the same chromaticity as the phosphor does. The McCamy formula is followed to determine the CCT of the light emitted from the synthesized material:[51]

$$\mathrm{CCT} = -449n^3 + 3525n^2 - 6823n + 5520.33 \quad (4)$$

where $n = (x - x_e)/(y - y_e)$ and x_e = 0.3320 and y_e = 0.1858. The computed values for color coordinates and correlated color temperature (CCT) are determined to be approximately x = 0.2339, y = 0.7414, and CCT = 6832 K for DC, and x = 0.2736, y = 0.6947, and CCT = 6344 K for UC. The fact that the CCT values exceed 5000 K indicates that the suggested material has the potential to be a green phosphor suitable for cold white-LEDs.

To investigate the UC mechanisms involved, a pump power-dependent UC analysis was performed on phosphorus

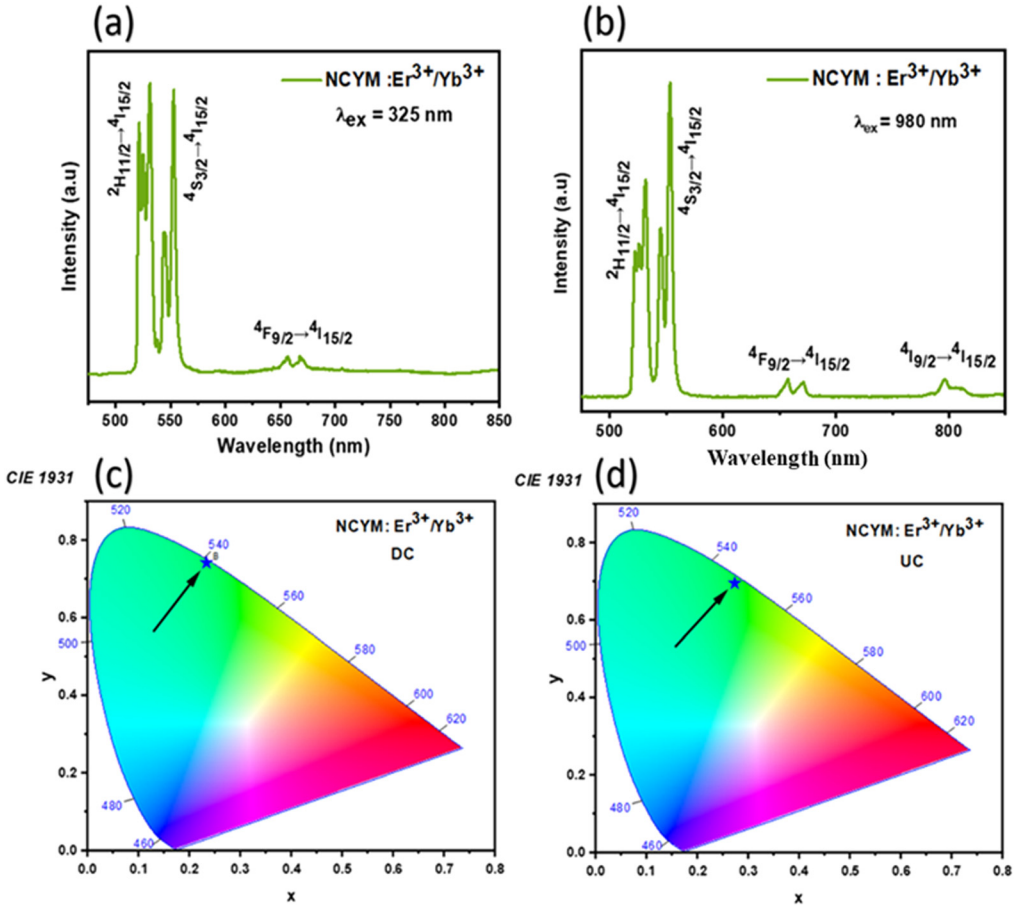

Fig. 4 (a) and (b) Emission spectra of NCYM:Er^{3+}/Yb^{3+} under 325 nm and 980 nm excitation, respectively. (c) and (d) CIE chromaticity coordinates of the phosphors.

NCYM:Er^{3+}/Yb^{3+}, as shown in Fig. 5. The UC emission intensity is related to the excitation power according to the following equation:[52,53]

$$I \propto P^n \quad (5)$$

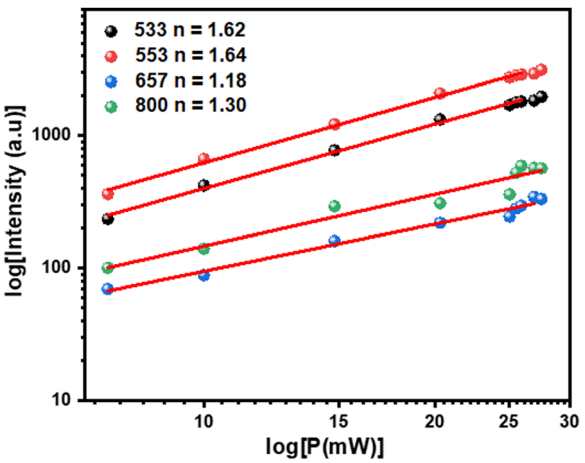

Fig. 5 Dependence of log(I_{UC}) on log(P) for 531, 553, 657 and 800 nm emissions of Er^{3+}.

In this context, I represents the integrated intensity of the up-conversion (UC) emission, P is the laser excitation power, and n is the number of excitation photons absorbed to emit the UC radiation. The slope of the fitted line in a log–log plot of I *versus* P provides the number of absorbed photons required for the UC process. For a two-photon process, the value of n typically ranges between 1 and 2. The slopes of the fitted lines corresponding to the integrated intensities of the green and red emissions for Er^{3+}/Yb^{3+} co-doped NCYM are 1.62, 1.64, 1.18, and 1.30, respectively. The n values indicate that all of the UC emission bands arise due to the cumulative absorption of the two photons. However, the values deviate from the exact value of 2 because of other processes like nonradiative relaxation (NRR) and energy transfer.

To gain a better understanding of the mechanism involved in light emission *via* UC emission modes, a study of the lifetime was carried out. The decay time was estimated by fitting the observed emission decay profiles with the simple exponential function mentioned below:[54,55]

$$I(t) = A + I_0 e^{(-t/\tau)} \quad (6)$$

where $I(t)$ represents the emission intensity at time t, I_0 refers to the initial emission intensity, A is a constant, and τ is the decay

lifetime. The temporal dependence of the green up-conversion (UC) emission under pulsed irradiation at 980 nm is shown in Fig. S3 (ESI†). The observed rise time of the curve indicates that energy transfer processes are required to populate the green-emitting levels. The decay time (τ = 0.18 μs) was determined using eqn (6).

Based on the photoluminescence properties observed in the visible and red regions, and the analysis of the UC emission process, a proposed energy level diagram for NCYM co-doped with Er^{3+}/Yb^{3+} was built up, as shown in Fig. 6. Therein the emission mechanisms for both UC and DC processes are described in detail.

Under 325 nm excitation (DC), the molybdate ion in its ground state $^1A_1$ can be excited to the $^1T_2$ state, and then relaxes non-radiatively to the $^1T_1$ state. The excited energy level $^1T_1$ of the molybdate is nearly aligned with the excitable $^4G_{11/2}$ state of Er^{3+}, leading to a non-radiative resonance energy transfer from the molybdate to the Er^{3+} ions. The excited $^4G_{11/2}$ state of Er^{3+} undergoes non-radiative relaxation to the emitting $^2H_{11/2}$, $^4S_{3/2}$, and $^4F_{9/2}$ states of Er^{3+}, resulting in green and red emissions at 533, 553, and 657 nm, respectively, thus explaining the DC mechanism.[56–59]

The UC mechanisms of the green and red emissions of Er^{3+} ions in the co-doped Er^{3+}/Yb^{3+} NCYM follow the absorption of two photons. This result is similar to that of Er^{3+}/Yb^{3+} doping in various other media, such as $NaYF_4$ glass ceramic,[60] $NaYF_4$,[61] Y_2O_3,[62] SnO_2,[63] TiO_2,[64] and so on. Green light is emitted from the excited states $^2H_{11/2}$ and $^4S_{3/2}$. First, the electrons transit from the $^4I_{15/2}$ ground state to the $^4I_{11/2}$ state *via* ground state absorption (GSA), followed by excited state absorption (ESA1) to the $^4F_{7/2}$ state. Then, by multi-phonon relaxation, they reach the $^2H_{11/2}$ and $^4S_{3/2}$ states, and emit green light by decaying to the $^4I_{15/2}$ ground state. Simultaneously, the red emission is linked to the population of the $^4F_{9/2}$ state. NCYM co-doped Er^{3+}/Yb^{3+} and Yb^{3+} ions are excited from the ground state to the $^2F_{5/2}$ level under excitation with 980 nm by GSA ($^2F_{7/2} \rightarrow {}^2F_{5/2}$). As Yb^{3+} ions have a much larger absorption cross section than Er^{3+} ions in the 980 nm spectral range, the ET process becomes dominant over GSA for excitation of the Er^{3+} $^4I_{11/2}$ level. A second Yb^{3+} ion transfers its energy to the $^4I_{11/2}$ level to populate the $^4F_{7/2}$ Er^{3+} level, which then de-excites to the $^2H_{11/2}$, $^4S_{3/2}$, $^4F_{9/2}$ and $^4I_{9/2}$ levels.[65,66] At the end of these UC processes, green and red emissions are obtained by up-conversion. Yb^{3+} acts as a sensitizer and enriches the population of all emitting levels by transferring their absorbed energy to the activating ion.

4.3 Temperature sensing properties of NCYM:Er^{3+}/Yb^{3+} (DC)

To evaluate the potential application of the Er^{3+}/Yb^{3+} co-doped NCYM phosphor in optical thermometry, the temperature-dependent luminescence behavior of the sample was studied in detail under 325 nm excitation. Fig. 7 illustrates the temperature-dependent emission spectra in the range of 450–850 nm for the NCYM:Er^{3+}/Yb^{3+} phosphor excited at 325 nm. The obtained spectra show two peaks attributed to the Er^{3+} ion transitions, located in the green visible region: 533 nm ($^2H_{11/2} \rightarrow {}^4I_{15/2}$) and 553 nm ($^4S_{3/2} \rightarrow {}^4I_{15/2}$), along with a relatively weaker red band centered at 657 nm, attributed to the $^4F_{9/2} \rightarrow {}^4I_{15/2}$ transition of Er^{3+} ions. Compared to the $^4S_{3/2} \rightarrow {}^4I_{15/2}$ transition, the emission intensity of the $^2H_{11/2} \rightarrow {}^4I_{15/2}$ transition exhibits a monotonic increase with no apparent shift in the band position as the temperature rises. This indicates that the $^2H_{11/2}$ level can be effectively populated from the $^4S_{3/2}$ level through a thermal excitation process.[67] Furthermore, the increase in temperature is also beneficial in reducing structural defects and surface ligands. Therefore, the thermally coupled levels (TCLs) method is assumed to be applicable for optical thermometry.

Among the various techniques used to study temperature-sensing behavior, the luminescence intensity ratio (LIR) technique is widely recognized. Several studies have investigated the temperature sensing behavior of different rare-earth doped materials using the LIR technique. As the temperature increases, the peak positions of the emission bands remain

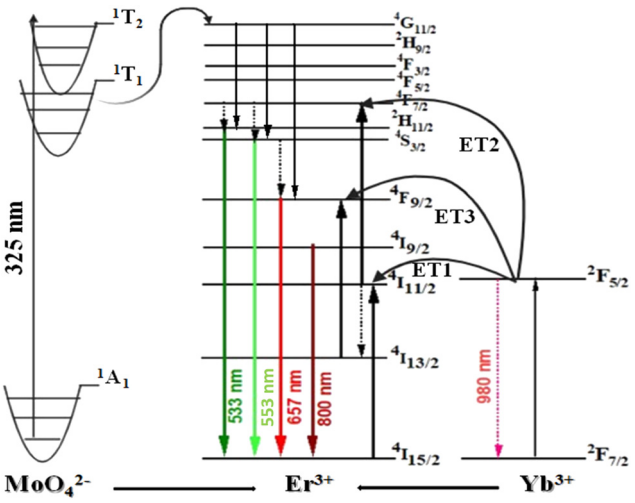

Fig. 6 Energy level diagram and the proposed DC and UC mechanism for the Er^{3+}/Yb^{3+}-co-doped NCYM.

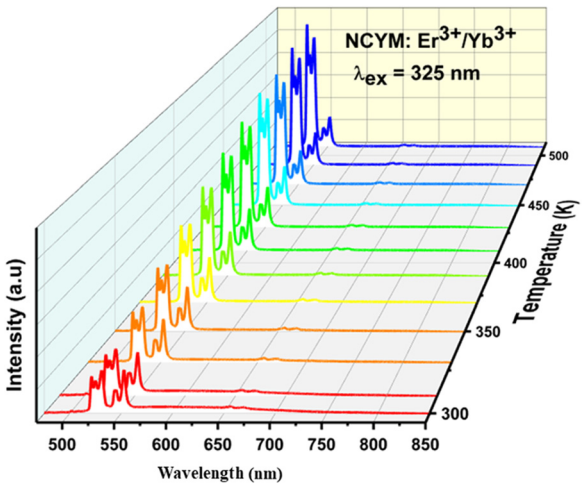

Fig. 7 DC emission spectra of the Er^{3+}/Yb^{3+} co-doped NCYM sample measured under 325 nm laser irradiation in the 300 to 510 K temperature range.

unchanged; however, the intensities of the bands change, resulting in variations in the luminescence intensity ratio (LIR) between the 533 nm and 553 nm bands. The LIR varies according to the following relationship:[68,69]

$$\mathrm{LIR} = \frac{I_H}{I_S} = A \times \exp\left(\frac{-\Delta E}{k_B T}\right) \quad (7)$$

where I_H and I_S are the integrated intensities corresponding to the two green bands, 533 nm and 553 nm, respectively. A is a constant of proportionality, ΔE is the energy difference between the thermally coupled $^4S_{3/2}$ and $^2H_{11/2}$ levels, and k_B = 0.695 cm^{-1} is the Boltzmann constant. The linear fitting of the experimental data yields a slope value of approximately 1086.25, which corresponds to the $\Delta E/k_B$ value. From this value, the calculated ΔE is approximately 754.94 cm^{-1}. The LIR of the 533 nm and 553 nm emission bands as a function of temperature in the 300–510 K temperature range is plotted in Fig. 8(a). The LIR varies from 0.81 to 3.55 within this temperature range. The data exhibit an excellent fit to the model, with a high correlation coefficient (R^2 = 0.993). It is important to assess the sensitivity (S_r and S_a) of the material, which quantifies the rate at which the LIR changes with temperature. Absolute thermal sensitivity demonstrates the absolute change in LIR as a function of temperature, and is defined as follows:[70,71]

$$S_a = \frac{d\mathrm{LIR}}{dT} \quad (8)$$

It is clear that the absolute thermal sensitivity (S_a) depends on the absolute magnitude of the LIR, which can be easily modified by manipulating the methodology for calculating the LIR (such as widening the spectral limits for calculating the integral intensity). The concept of relative thermal sensitivity was introduced to ensure a fair assessment of the performance of thermometers, irrespective of their inherent characteristics and detection parameters. The normalized change in LIR as a function of temperature variation is indicated by the relative sensitivity.[72,73]

$$S_r = \frac{1}{\mathrm{LIR}} \times \frac{d\mathrm{LIR}}{dT} \quad (9)$$

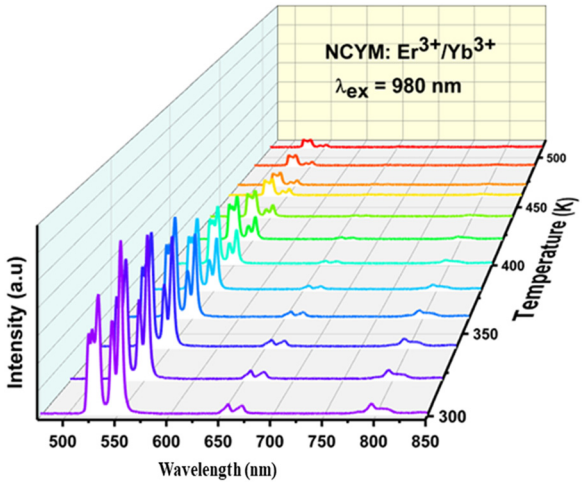

Fig. 9 UC emission spectra of the Er^{3+}/Yb^{3+}-co-doped NCYM sample measured under 980 nm laser irradiation in the temperature range from 300 to 510 K.

Fig. 8(b) shows the temperature-dependent changes in S_a and S_r values over the temperature range from 300 to 510 K for LIR. The maximum value of relative sensitivity (S_r) is observed to be 1.2% K^{-1} at 300 K, while the absolute sensitivity (S_a) is estimated to be 15.17 × 10^{-3} K^{-1} at 510 K.

4.4 Temperature sensing properties of NCYM:Er^{3+}/Yb^{3+} (UC)

The optical temperature sensing capability was also investigated in this case by measuring the temperature-dependent UC emission spectra of NCYM:Er^{3+}/Yb^{3+} in the 450–850 nm range. Fig. 9 shows the UC emission spectra of the Er^{3+}/Yb^{3+} co-doped NCYM material at different temperatures. Luminescence emission intensity is highly dependent on temperature.

To minimize the potential effects of temperature increase during high power density excitations, appropriate measures must be implemented. It is essential to maintain relatively low power levels in LIR thermometry to mitigate self-heating effects. Consequently, the spectra were acquired at different

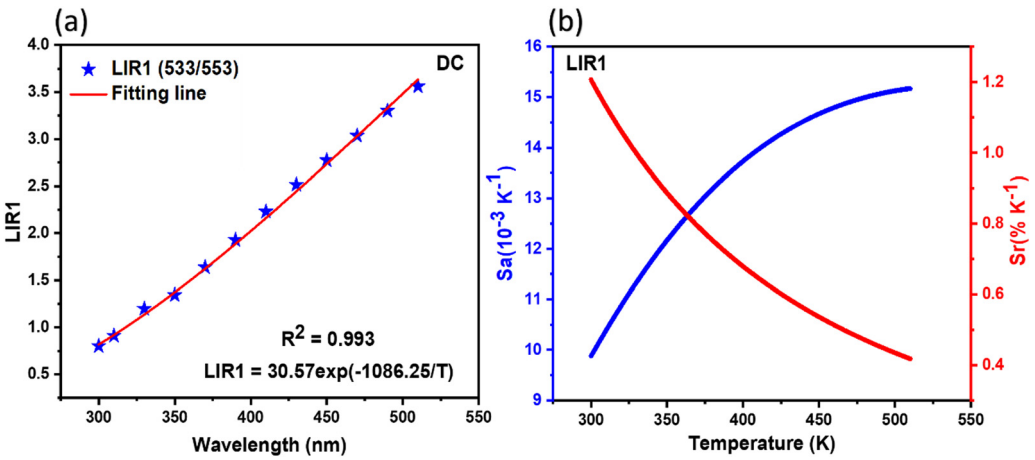

Fig. 8 (a) and (b) Temperature dependence of the LIR1 value between $^2H_{11/2}$ and $^4S_{3/2}$ TCL of Er^{3+} ions, and (b) the calculated S_r and S_a by LIR1 from TCL based on down-conversion.

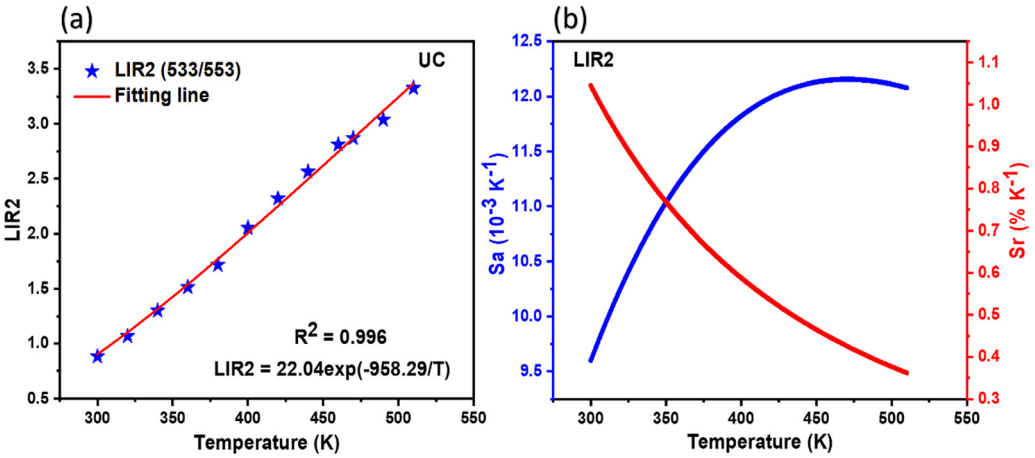

Fig. 10 (a) and (b) Temperature dependence of the LIR2 value between $^2H_{11/2}$ and $^4S_{3/2}$ TCL of Er^{3+} ions, and (b) the calculated S_r and S_a by LIR2 from TCL based on up-conversion.

powers of the excitation laser, selecting the maximum power at which there are no spectral changes, thus the measurements were carried out with a pump power of 30 mW, corresponding to a power density of 0.2 W cm^{-2}.

It was observed that most of the emissions from the sample, except for the emissions at 533 nm, decreased with increasing temperature. As the temperature rises, the lattice vibrations are enhanced and accelerate the rate of non-radiative relaxation between closely spaced energy levels. This process leads to thermal equilibrium between the energy levels, suggesting that the $^2H_{11/2}$ and $^4S_{3/2}$ states are thermally coupled. The relative population of the two thermally coupled electronic states can be mathematically described using the Boltzmann-distribution law, as defined previously.

The calculated LIR values, as shown in Fig. 10(a), are in good agreement with the Boltzmann-distribution. The LIR was calculated using eqn (7). LIR values for the thermally coupled levels $^2H_{11/2} \rightarrow {}^4I_{15/2}$ and $^4S_{3/2} \rightarrow {}^4I_{15/2}$ (LIR2 = 533/553 nm) were determined and presented in Fig. 10(a). The LIR data fit very well, with a high degree of correlation (R^2 = 0.996).

The performance of the thermometer was further assessed using both the absolute and relative thermal sensitivity, as previously defined (eqn (8) and (9)). Fig. 10(b) displays the temperature-dependent variations in the values of S_a and S_r over the range from 300 to 510 K for LIR2. The observed data reveal contrasting trends for the absolute and relative sensitivities as a function of temperature. The study indicated that the highest absolute sensitivities occurred at different temperatures, with a maximum value of 12.15 × 10^{-3} K^{-1} observed at room temperature for LIR2. In contrast, the relative sensitivity (S_r) decreases with increasing temperature, reaching its maximum value of 1.045% K^{-1} at 300 K (Fig. 10(b)).

Finally, aiming to provide the reader with an understanding of the current state of the art, a summary of various luminescent thermometers based on up/down conversion is presented in Table 1. It can be concluded that, in comparison with the detection sensitivity of other phosphors based on TCLs ($^2H_{11/2}$/$^4S_{3/2}$), our phosphor demonstrates superior performance using both methods.

Temperature resolution, also known as uncertainty (δT), is another key parameter that determines the smallest temperature change that can be detected by an optical thermometer. It also describes the possible error in temperature readings. The temperature uncertainty (δT) using luminescent thermometry can be

Table 1 Comparison of the observed temperature-sensing performance parameter with other phosphor samples for temperature-sensing applications

Samples	Temperature range (K)	$S_{r\text{-max}}$ (% K^{-1})	Excitation (nm)	Ref.
$Ca_2MgWO_6:Yb^{3+}/Er^{3+}$	300–600	0.92 (at 303 K)	980	74
$La_2O_3:Er^{3+}/Yb^{3+}$	303–600	0.91 (at 303 K)	980	75
$BiVO_4:Er^{3+}/Yb^{3+}$	283–483	1.39 (at 283 K)	980	76
$KYb_2F_7:Er^{3+}$	300–480	0.45 (at 300 K)	980	77
Sr2YbF7:Er^{3+}	300–500	0.62 (at 300 K)	980	78
$SrMoO_4:Er^{3+}/Yb^{3+}$	300–543	1.18 (at 300 K)	980	79
$LaGdO_3:Er^{3+}/Yb^{3+}$	283–393	1.27 (at 283 K)	980	80
$NaBiF_4:Er^{3+}/Yb^{3+}$	248–498	0.40 (at 498 K)	980	81
β-NaYF4:Er^{3+}/Yb^{3+}	303–678	0.30 (at 580 K)	980	82
YOF:Er^{3+}/Yb^{3+}	260–490	0.60 (at 490 K)	980	83
$LaGdO_3:Er^{3+}$	298–873	0.43 (at 300 K)	488	84
$La_2MoO_6:Er^{3+}$	303–463	0.97 (at 480 K)	379	85
NCYM:Er^{3+}/Yb^{3+}	**300–510**	**1.20 (at 300 K)**	**325**	**This Work**
NCYM:Er^{3+}/Yb^{3+}	**300–510**	**1.04 (at 300 K)**	**980**	**This Work**

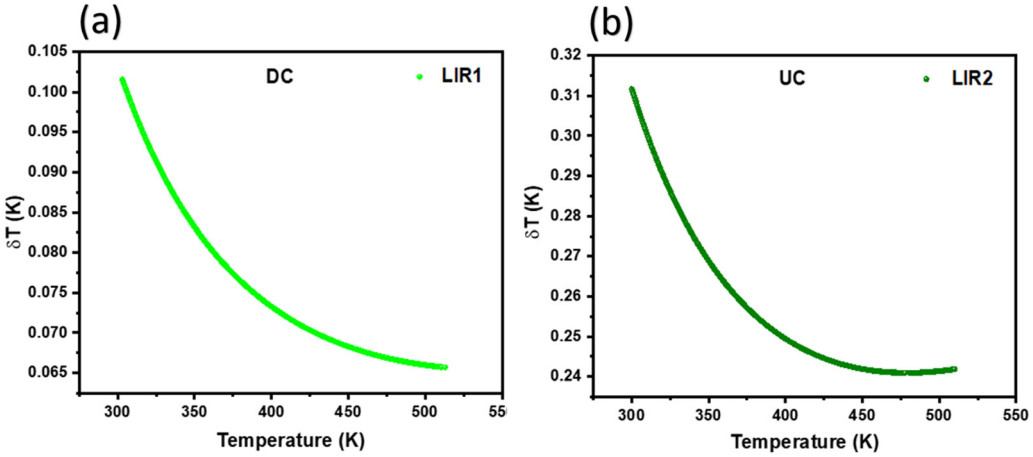

Fig. 11 (a)–(d) Temperature resolution values, δT, corresponding to (a) LIR1 (DC) and (b) LIR2 (UC) for NCYM:Er^{3+}/Yb^{3+}.

calculated using the equation as follows:[23,59,86]

$$\delta T = \frac{1}{S_r}\frac{\delta \mathrm{FIR}}{\mathrm{FIR}} \quad (10)$$

In this study, the LIR uncertainty (δLIR) was calculated using the standard deviation of multiple measurements at a fixed temperature, with the LIR being the mean value of these measurements. To determine the detection limit, 50 measurements were taken at room temperature under consistent conditions. The results are shown in the histograms in Fig. S4(a) and (b) (ESI†). The LIR uncertainty (δLIR) for the NCYM:Er^{3+}/Yb^{3+} phosphor was found to be 0.001 and 0.003 for LIR1 and LIR2, respectively. By applying eqn (10), the uncertainty in temperature (δT), as shown in Fig. 11(a) and (b), was found to be below 0.313 K. These findings demonstrate that the NCYM-based phosphor exhibits excellent temperature resolution within its operational range, surpassing the performance of $NaYF_4$:Yb^{3+}/Er^{3+}, YPO_4:Yb^{3+}/Er^{3+} phosphors, and tellurite glass ceramics doped with Yb^{3+}/Er^{3+}.

Overall, our results suggest that NCYM materials, which utilize both up-conversion and down-conversion processes, exhibit high thermal sensitivity and low measurement uncertainty, making them highly promising for optical thermometry applications using the LIR approach.

5. Conclusions

NCYM phosphors co-doped with Er^{3+}/Yb^{3+}, emitting in dual modes, were successfully synthesized using the sol–gel method. X-ray diffraction (XRD) and Rietveld refinement confirm that all prepared phosphors exhibit a pure phase with a tetragonal scheelite structure (space group $I4_1/a$). The phosphors show intense green and red light emissions due to the electronic transitions of Er^{3+} ions, including $^2H_{11/2} \rightarrow {}^4I_{15/2}$, $^4S_{3/2} \rightarrow {}^4I_{15/2}$, $^4F_{9/2} \rightarrow {}^4I_{15/2}$, and $^4I_{9/2} \rightarrow {}^4I_{15/2}$ under both near UV (325 nm) and NIR (980 nm) excitation. The chromaticity coordinates are in the green region, with CIE coordinates (x = 0.2339; y = 0.7414) for down-conversion (DC) and (x = 0.2736; y = 0.6947) for up-conversion (UC). The power-dependent UC emission analysis reveals that two photons are involved in the UC emission process. The luminescence intensity ratio (LIR) of the green bands corresponding to the $^2H_{11/2} \rightarrow {}^4I_{15/2}$ and $^4S_{3/2} \rightarrow 4I_{15/2}$ transitions were studied as a function of temperature to assess their potential for temperature sensing. Maximum sensitivity values were found to be 1.2% K^{-1} and 1.045% K^{-1} at 300 K for DC and UC, respectively. The luminescence thermometry results demonstrated excellent temperature accuracy, with a calculated temperature uncertainty (δT) of less than 0.313 K. These findings underscore the remarkable potential of NCYM:Yb^{3+}/Er^{3+} phosphors as optical temperature sensors, offering high sensitivity and a broad temperature detection range in both DC and UC modes.

Data availability

All data underlying the results are available as part of the article and no additional source data are required.

Conflicts of interest

There are no conflicts to declare.

References

1 Y. Chen, *et al.*, Temperature-dependent luminescence of Bi^{3+}, Eu^{3+} co-activated La_2MgGeO_6 phosphor for dual-mode optical thermometry, *J. Lumin.*, 2022, **249**, 118995.
2 M. Pokhrel, *et al.*, Up- and Down-Convertible LaF_3:Yb,Er Nanocrystals with a Broad Emission Window from 350 nm to 2.8 μm: Implications for Lighting Applications, *ACS Appl. Nano Mater.*, 2021, **4**, 13562–13572.
3 P. Singh, *et al.*, Lanthanide doped ultrafine hybrid nanostructures: multicolour luminescence, upconversion based energy transfer and luminescent solar collector applications, *Nanoscale*, 2017, **9**, 696–705.
4 Y. Zhou, *et al.*, Abnormal thermally enhanced upconversion luminescence of lanthanide-doped phosphors: proposed

mechanisms and potential applications, *J. Mater. Chem. C*, 2021, **9**, 2220–2230.
5 F. Jahanbazi and Y. Mao, Recent advances on metal oxide-based luminescence thermometry, *J. Mater. Chem. C*, 2021, **9**, 16410–16439.
6 L. Huang, *et al.*, Near-Infrared Persistent Luminescence in a Cr^{3+}-Doped Perovskite for Low-Irradiance Imaging, *Chem. Mater.*, 2020, **32**, 5579–5588.
7 Z. Tang, G. Zhang and Y. Wang, Design and Development of a Bluish-Green Luminescent Material ($K_2HfSi_3O_9$:Eu^{2+}) with Robust Thermal Stability for White Light-Emitting Diodes, *ACS Photonics*, 2018, **5**, 3801–3813.
8 Q. Tang, *et al.*, Luminous tuning in Eu^{3+}/Mn^{4+} co-doped double perovskite structure by designing the site-occupancy strategy for solid-state lighting and optical temperature sensing, *Mater. Res. Bull.*, 2022, **149**, 111704.
9 N. B. Amar, K. Saidi, C. Hernández-Álvarez, M. Dammak and I. R. Martin, Ultra-high-sensitive temperature sensing based on emission Pr^{3+} and Yb^{3+} codoped $Y_2Mo_3O_{12}$ nanostructures, *Mater. Adv.*, 2024, **6**, 827–838.
10 M. Fhoula, *et al.*, Unlocking the luminescent potential of Pr^{3+}/Yb^{3+} Co-doped $Y_2Mo_4O_{15}$ for advanced thermometry applications, *J. Alloys Compd.*, 2024, **979**, 173537.
11 I. Kachou, K. Saidi, C. Hernández-Álvarez, M. Dammak and I. R. Martín, Enhancing thermometric precision: modulating the temperature of maximum sensitivity via erbium dopant addition in $Ba_2GdV_3O_{11}$:Tm^{3+}/Yb^{3+} nano phosphors, *Mater. Adv.*, 2024, **5**, 8280–8293.
12 K. Saidi, M. Dammak, K. Soler-Carracedo and I. R. Martín, A novel optical thermometry strategy based on emission of Tm^{3+}/Yb^{3+} codoped $Na_3GdV_2O_8$ phosphors, *Dalton Trans.*, 2022, **51**, 5108–5117.
13 F. Ayachi, K. Saidi, M. Dammak, I. Mediavilla and J. Jiménez, Unlocking advanced thermometric capabilities: $BiVO_4$:Er^{3+}/Yb^{3+} nanophosphors with dual-mode up-conversion and down-shifting features, *RSC Adv.*, 2025, **15**, 655–664.
14 M. Fhoula, M. Khitouni and M. Dammak, Comparative optical thermometry analysis using $Na_2SrP_2O_7$:Er^{3+}/Yb^{3+} phosphors: evaluation of LIR TCL and LIR NTCL methods for high-resolution temperature sensing, *RSC Adv.*, 2024, **14**, 39373–39380.
15 I. Kachou, *et al.*, Advanced temperature sensing with Er^{3+}/Yb^{3+} co-doped $Ba_2GdV_3O_{11}$ phosphors through upconversion luminescence, *Dalton Trans.*, 2024, **53**, 2357–2372.
16 K. Saidi, C. Hernández-Álvarez, M. Runowski, M. Dammak and I. Rafael Martín Benenzuela, Temperature and Pressure Sensing Using an Optical Platform Based on Upconversion Luminescence in $NaSrY(MoO_4)_3$ Codoped with Er^{3+} and Yb^{3+} Nanophosphors, *ACS Appl. Nano Mater.*, 2023, **6**, 19431–19442.
17 K. Saidi, I. Kachou, K. Soler-Carracedo, M. Dammak and I. R. Martín, $Ba_2YV_3O_{11}$ Er^{3+}/Yb^{3+} Nanostructures for Temperature Sensing in the Presence of Bismuth Ions, *ACS Appl. Nano Mater.*, 2023, **6**, 17681–17690.
18 K. Saidi, C. Hernández-Álvarez, M. Runowski, M. Dammak and I. R. Martín, Ultralow pressure sensing and luminescence thermometry based on the emissions of Er^{3+}/Yb^{3+} codoped $Y_2Mo_4O_{15}$ phosphors, *Dalton Trans.*, 2023, **52**, 14904–14916.
19 N. M. Bhiri, *et al.*, Excitation power density dependence of a primary luminescent thermometer based on Er^{3+},Yb^{3+}:$GdVO_4$ microcrystals operating in the visible, *J. Alloys Compd.*, 2022, **921**, 166020.
20 N. M. Bhiri, *et al.*, Stoichiometric dependence and laser heating effect on the luminescence thermometric performance of Er^{3+}, Yb^{3+}:$YuGdwVO_4$ microparticles in the non-saturation regime, *Mater. Res. Bull.*, 2022, **151**, 111801.
21 F. Ayachi, K. Saidi, W. Chaabani and M. Dammak, Synthesis and luminescence properties of Er^{3+} doped and Er^{3+}–Yb^{3+} codoped phosphovanadate $YP_{0.5}V_{0.5}O_4$ phosphors, *J. Lumin.*, 2021, **240**, 118451.
22 K. N. Kumar, G. Kang, J. Lim and J. Choi, Biocompatible Yb^{3+}/Er^{3+} Co-activated $La_2(WO_4)_3$ Upconversion Nanophosphors for Optical Thermometry, Biofluorescent, and Anticancer Agents, *Inorg. Chem.*, 2022, **61**, 3851–3865.
23 F. Ayachi, *et al.*, Dual-mode luminescence of Er^{3+}/Yb^{3+} codoped $LnP_{0.5}V_{0.5}O_4$ (Ln = Y, Gd, La) for highly sensitive optical nanothermometry, *Mater. Today Chem.*, 2023, **27**, 101352.
24 K. Pavani, *et al.*, Highly efficient upconversion of Er^{3+} in Yb^{3+} codoped non-cytotoxic strontium lanthanum aluminate phosphor for low temperature sensors, *Sci. Rep.*, 2017, **7**, 17646.
25 C. Hernández-Álvarez, *et al.*, Multifunctional optical sensing platform of temperature, pressure (vacuum) and laser power density: $NaYF_4$:Gd^{3+},Yb^{3+},Er^{3+} nanomaterial as luminescent thermometer, manometer and power meter, *J. Mater. Chem. C*, 2023, **11**, 10221–10229.
26 S. Tomar, *et al.*, Dual-Mode Light Emission and Dynamic Studies of Er^{3+}/Yb^{3+}-Doped $NaLa(MoO_4)_2$ Phosphor for Optical Thermometry Operating from Cryogenic to above Room Temperatures, *ACS Appl. Opt. Mater.*, 2024, **2**, 1965–1984.
27 S. K. Singh, K. Kumar and S. B. Rai, Diode laser pumped Gd_2O_3:Er^{3+}/Yb^{3+} phosphor as optical nano-heater, *Appl. Phys. B: Lasers Opt.*, 2010, **100**, 443–446.
28 A. K. Singh, *et al.*, Light-into-heat conversion in La_2O_3:Er^{3+}–Yb^{3+} phosphor: an incandescent emission, *Opt. Lett.*, 2012, **37**, 776–778.
29 S. K. Singh, K. Kumar and S. B. Rai, Multifunctional Er^{3+}–Yb^{3+} codoped Gd_2O_3 nanocrystalline phosphor synthesized through optimized combustion route, *Appl. Phys. B: Lasers Opt.*, 2009, **94**, 165–173.
30 X. He, J. Zhou, N. Lian, J. Sun and M. Guan, Sm^{3+}-activated gadolinium molybdate: an intense red-emitting phosphor for solid-state lighting based on InGaN LEDs, *J. Lumin.*, 2010, **130**, 743–747.
31 X. Zhao, *et al.*, Novel Eu^{3+}-doped red-emitting phosphor $Gd_2Mo_3O_9$ for white-light-emitting-diodes (WLEDs) application, *J. Alloys Compd.*, 2007, **433**, 352–355.
32 I. Kumar, *et al.*, Simultaneous realization of FIR-based multimode optical thermometry and photonic molecular

logic gates in Er^{3+} and Yb^{3+} co-doped $SrTiO_3$ phosphor, *Phys. Scr.*, 2023, **98**, 105532.

33 I. Kumar, *et al.*, Charge compensation-driven downconverted luminescence enhancement in Er^{3+}-doped $SrTiO_3$ phosphors by co-doping with alkali ions (M^+ = Li, Na, K) for solid-state lighting applications, *Indian J. Phys.*, 2024, 1–10, DOI: 10.1007/s12648-024-03432-9.

34 I. Kumar, *et al.*, NIR Light-triggered Green Emitting Perovskite-based Phosphor for Optical Thermometry and Future Molecular Logic Gate Applications, *J. Fluoresc.*, 2024, 1–13, DOI: 10.1007/s10895-024-04044-6.

35 I. Kumar, A. Kumar, S. Kumar, V. Sangwan and A. K. Gathania, Green Emission in Thermally Stable Er^{3+} Doped Lead-Free Perovskite Phosphor for Solid-State Lighting and Optical Thermometry Applications, *IEEE Photonics J.*, 2024, **16**, 1–7.

36 X. Chen, *et al.*, A multi-mode optical thermometer based on the up-conversion $Ca_3Y_2Ge_3O_{12}$:Er^{3+},Yb^{3+} phosphor, *J. Lumin.*, 2023, **261**, 119907.

37 Y. Bu, *et al.*, A dual-mode self-referenced optical thermometry with high sensitivity based on Er^{3+}–Yb^{3+} co-doped Sr_2YTaO_6 thermochromic phosphor, *J. Lumin.*, 2022, **248**, 118923.

38 A. Pandey, V. K. Rai, V. Kumar, V. Kumar and H. C. Swart, Upconversion based temperature sensing ability of Er^{3+}–Yb^{3+} codoped $SrWO_4$: an optical heating phosphor, *Sens. Actuators, B*, 2015, **209**, 352–358.

39 M. Runowski, P. Woźny, S. Lis, V. Lavín and I. R. Martín, Optical Vacuum Sensor Based on Lanthanide Upconversion—Luminescence Thermometry as a Tool for Ultralow Pressure Sensing, *Adv. Mater. Technol.*, 2020, **5**, 1901091.

40 F. Paz-Buclatin, *et al.*, $GdVO_4$:Er^{3+}/Yb^{3+} nanocrystalline powder as fluorescence temperature sensor. Application to monitor the temperature of an electrical component, *Sens. Actuators, A*, 2019, **299**, 111628.

41 J. Liu, *et al.*, Synthesis and luminescence properties of $CaMoO_4$:Er^{3+}/Yb^{3+} nanoparticles, *J. Mater. Sci.: Mater. Electron.*, 2015, **26**, 3380–3383.

42 A. Kumar and J. Manam, Optical thermometry using up and down conversion photoluminescence mechanism in $Y_2Zr_2O_7$:Er^{3+} phosphors with excellent sensing sensitivity, *J. Alloys Compd.*, 2020, **829**, 154610.

43 M. Wei, *et al.*, Albumin assisted sol-gel synthesized $SrSnO_3$:Pr^{3+} red persistent phosphors for temperature sensing, *J. Lumin.*, 2021, **239**, 118328.

44 X. Yang, *et al.*, Optical Temperature Sensing Behavior of High-Efficiency Upconversion: Er^{3+} –Yb^{3+} Co-Doped $NaY(MoO_4)_2$ Phosphor, *J. Am. Ceram. Soc.*, 2015, **98**, 2595–2600.

45 Z. E. A. A. Taleb, K. Saidi and M. Dammak, High-precision optical thermometry using Pr^{3+}-doped $NaCaY(MoO_4)_3$ luminophores: a multi-spectral and chromaticity-based approach to non-contact temperature sensing, *RSC Adv.*, 2025, **15**, 5327–5337.

46 M. Enneffati, M. Rasheed, B. Louati, K. Guidara and R. Barillé, Morphology, UV-visible and ellipsometric studies of sodium lithium orthovanadate, *Opt. Quantum Electron.*, 2019, **51**, 299.

47 Y. Jiang, *et al.*, A three-mode self-referenced optical thermometry based on up-conversion luminescence of Ca_2MgWO_6:Er^{3+},Yb^{3+} phosphors, *Chem. Eng. J.*, 2021, **413**, 127470.

48 S. Tabanli and G. Eryurek, Optical investigation of Er^{3+} and Er^{3+}/Yb^{3+} doped zinc-tellurite glass for solid-state lighting and optical thermometry, *Sens. Actuators, A*, 2019, **285**, 448–455.

49 S. Agrawal and V. Dubey, Down conversion luminescence behavior of Er and Yb doped Y_2O_3 phosphor, *J. Radiat. Res. Appl. Sci.*, 2014, **7**, 601–606.

50 K. Saidi, *et al.*, Multifunctional Optical Sensing with Lanthanide-Doped Upconverting Nanomaterials: Improving Detection Performance of Temperature and Pressure in the Visible and NIR Ranges, *ACS Appl. Mater. Interfaces*, 2024, **16**, 19137–19149.

51 I. Kachou, K. Saidi, R. Salhi and M. Dammak, Synthesis and optical spectroscopy of $Na_3Y(VO_4)_2$:Eu^{3+} phosphors for thermometry and display applications, *RSC Adv.*, 2022, **12**, 7529–7539.

52 S. Su, *et al.*, KYb_2F_7:Er^{3+} based nanothermometers: controlled synthesis, enhanced red emission, and improved sensitivities via crystal-site engineering, *J. Mater. Chem. C*, 2023, **11**, 2375–2388.

53 V. Kesarwani and V. K. Rai, Fluorescence intensity ratio technique and its reliability, *Methods Appl. Fluoresc.*, 2022, **10**, 034006.

54 M. M. Upadhyay, N. K. Mishra and K. Kumar, Upconversion luminescence based temperature sensing properties and anti-counterfeiting applications of $GdNbO_4$:Tm^{3+}/Yb^{3+} phosphor, *Spectrochim. Acta, Part A*, 2024, **304**, 123333.

55 Z. E. A. A. Taleb, K. Saidi, M. Dammak, D. Przybylska and T. Grzyb, Ultrasensitive optical thermometry using Tb^{3+} doped $NaSrGd(MoO_4)_3$ based on single band ratiometric luminescence, *Dalton Trans.*, 2023, **52**, 4954–4963.

56 K. Bouras, *et al.*, Photon management properties of Yb-doped SnO_2 nanoparticles synthesized by the sol–gel technique, *Phys. Chem. Chem. Phys.*, 2019, **21**, 21407–21417.

57 H. Cui, *et al.*, Extremely intense green up-conversion luminescent and ultra-high temperature sensitivity in Er^{3+}/Yb^{3+} co-doped $BiTa_7O_{19}$ phosphors, *J. Lumin.*, 2022, **241**, 118484.

58 Y. Chen, *et al.*, Up-conversion luminescence and temperature sensing properties based on Y_2GeO_5:Er^{3+},Yb^{3+} phosphors for three-mode optical thermometry, *J. Lumin.*, 2022, **250**, 119121.

59 Z. E. A. A. Taleb, K. Saidi and M. Dammak, The dual-model up/down-conversion green luminescence of $NaSrGd(MoO_4)_3$:Er^{3+} and its application for temperature sensing, *RSC Adv.*, 2024, **14**, 8366–8377.

60 X. Li, L. Yang, Y. Zhu, J. Zhong and D. Chen, Upconversion of transparent glass ceramics containing β-$NaYF_4$:Yb^{3+},Er^{3+} nanocrystals for optical thermometry, *RSC Adv.*, 2019, **9**, 7948–7954.

61 J. Zhao, *et al.*, Upconversion luminescence with tunable lifetime in $NaYF_4$:Yb,Er nanocrystals: role of nanocrystal size, *Nanoscale*, 2013, **5**, 944–952.

62 C. D. Mayrinck, *et al.*, Downconversion and upconversion observed from Er^{3+}/Yb^{3+}/Eu^{3+} tri-doped-Y_2O_3 for application in energy conversion, *J. Alloys Compd.*, 2020, **816**, 152591.

63 C. T. M. Dung, L. Van Hieu, L. Q. Vinh and T. T. T. Van, Remarkable enhancement of Er^{3+} emission at 1.54 μm in Er/Yb co-doped SiO_2–SnO_2 glass-ceramics, *J. Alloys Compd.*, 2018, **757**, 489–495.

64 R. Salhi and J.-L. Deschanvres, Efficient green and red up-conversion emissions in Er/Yb co-doped TiO_2 nanopowders prepared by hydrothermal-assisted sol–gel process, *J. Lumin.*, 2016, **176**, 250–259.

65 S. Tabanli and G. Eryurek, Excitation power and Er^{3+} concentration effect on the color quality parameters in Y_2O_3:Er^{3+}/Yb^{3+}/Tm^{3+} nanophosphors, *J. Nanophotonics*, 2018, **12**, 026008.

66 J. Yang, *et al.*, Controllable Red, Green, Blue (RGB) and Bright White Upconversion Luminescence of Lu_2O_3:Yb^{3+}/Er^{3+}/Tm^{3+} Nanocrystals through Single Laser Excitation at 980 nm, *Chem. – Eur. J.*, 2009, **15**, 4649–4655.

67 W. Xu, *et al.*, Optical temperature sensing in Er^{3+}–Yb^{3+} codoped $CaWO_4$ and the laser induced heating effect on the luminescence intensity saturation, *J. Alloys Compd.*, 2017, **726**, 547–555.

68 Z. E. A. A. Taleb, K. Saidi and M. Dammak, Dual-mode optical ratiometric thermometry using Pr^{3+}-doped $NaSrGd(MoO_4)_3$ phosphors with tunable sensitivity, *Dalton Trans.*, 2023, **52**, 18069–18081.

69 V. Kesarwani and V. K. Rai, Non-contact optical thermometry via non-thermally coupled levels in upconverting glass, *J. Appl. Phys.*, 2022, **132**, 113102.

70 Z. Chen, *et al.*, Mn^{4+}-Activated Double-Perovskite-Type Sr_2LuNbO_6 Multifunctional Phosphor for Optical Probing and Lighting, *ACS Appl. Mater. Interfaces*, 2023, **15**, 28193–28203.

71 Y. Ding, B. So, J. Cao, F. Langenhorst and L. Wondraczek, Light Delivery, Acoustic Read-Out, and Optical Thermometry Using Ultrasound-Induced Mechanoluminescence and the Near-Infrared Persistent Luminescence of CaZnOS:Nd^{3+}, *Adv. Opt. Mater.*, 2023, **11**, 2300331.

72 P. Du, L. Luo and J. S. Yu, Energy Back Transfer Induced Color Controllable Upconversion Emissions in La_2MoO_6:Er^{3+}/Yb^{3+} Nanocrystals for Versatile Applications, *Part. Part. Syst. Charact.*, 2018, **35**, 1700416.

73 J. Drabik, R. Kowalski and L. Marciniak, Enhancement of the sensitivity of single band ratiometric luminescent nanothermometers based on Tb^{3+} ions through activation of the cross relaxation process|, *Sci. Rep.*, 2020, **10**, 11190.

74 Y. Jiang, *et al.*, A three-mode self-referenced optical thermometry based on up-conversion luminescence of Ca_2MgWO_6:Er^{3+},Yb^{3+} phosphors, *Chem. Eng. J.*, 2021, **413**, 127470.

75 R. Dey and V. K. Rai, Yb^{3+} sensitized Er^{3+} doped La_2O_3 phosphor in temperature sensors and display devices, *Dalton Trans.*, 2014, **43**, 111–118.

76 J. Sun, *et al.*, Temperature self-monitoring photothermal nano-particles of Er^{3+}/Yb^{3+} Co-doped zircon-tetragonal $BiVO_4$, *Ceram. Int.*, 2021, **47**, 409–415.

77 J. Cao, *et al.*, Optical thermometry based on up-conversion luminescence behavior of Er^{3+}-doped KYb_2F_7 nano-crystals in bulk glass ceramics, *J. Alloys Compd.*, 2017, **693**, 326–331.

78 X. Li, J. Cao, Y. Wei, Z. Yang and H. Guo, Optical Thermometry Based on Up-Conversion Luminescence Behavior of Er^{3+}-Doped Transparent Sr_2YbF_7 Glass-Ceramics, *J. Am. Ceram. Soc.*, 2015, **98**, 3824–3830.

79 X. Liu, *et al.*, Comparison study on the different strategies designed for ratiometric luminescence thermometry in Er^{3+}/Yb^{3+}:$SrMoO_4$ phosphor, *Sens. Actuators, A*, 2020, **315**, 112287.

80 A. Siaï, P. Haro-González, K. Horchani Naifer and M. Férid, Optical temperature sensing of Er^{3+}/Yb^{3+} doped $LaGdO_3$ based on fluorescence intensity ratio and lifetime thermometry, *Opt. Mater.*, 2018, **76**, 34–41.

81 O. A. Savchuk, J. J. Carvajal, C. Cascales, M. Aguiló and F. Díaz, Benefits of Silica Core–Shell Structures on the Temperature Sensing Properties of Er,Yb:$GdVO_4$ Up-Conversion Nanoparticles, *ACS Appl. Mater. Interfaces*, 2016, **8**, 7266–7273.

82 D. Chen, *et al.*, Bulk glass ceramics containing Yb^{3+}/Er^{3+}:β-$NaGdF_4$ nanocrystals: Phase-separation-controlled crystallization, optical spectroscopy and upconverted temperature sensing behavior, *J. Alloys Compd.*, 2015, **638**, 21–28.

83 H. Suo, *et al.*, Sensitivity Modulation of Upconverting Thermometry through Engineering Phonon Energy of a Matrix, *ACS Appl. Mater. Interfaces*, 2016, **8**, 30312–30319.

84 V. Gutiérrez-Cano, F. Rodríguez, J. A. González and R. Valiente, Upconversion and Optical Nanothermometry in $LaGdO_3$:Er^{3+} Nanocrystals in the RT to 900 K Range, *J. Phys. Chem. C*, 2019, **123**, 29818–29828.

85 P. Du and J. S. Yu, Near-ultraviolet light induced visible emissions in Er^{3+}-activated La_2MoO_6 nanoparticles for solid-state lighting and non-contact thermometry, *Chem. Eng. J.*, 2017, **327**, 109–119.

86 J. Stefanska, K. Maciejewska and L. Marciniak, Blue-emitting single band ratiometric luminescent thermometry based on LaF_3:Pr^{3+}, *New J. Chem.*, 2021, **45**, 11898–11904.